Geochemistry Geophysics Geosystems G3
AN ELECTRONIC JOURNAL OF THE EARTH SCIENCES
Published by AGU and the Geochemical Society

Article
Volume 11, Number 3
12 March 2010
Q03008, doi:10.1029/2009GC002836
ISSN: 1525-2027

Characterizing the 410 km discontinuity low-velocity layer beneath the LA RISTRA array in the North American Southwest

John J. Jasbinsek
Physics Department, California Polytechnic State University, San Luis Obispo, California 93407, USA (jjasbins@calpoly.edu)

Ken G. Dueker and Steven M. Hansen
Department of Geology and Geophysics, University of Wyoming, Laramie, Wyoming 82071, USA

[1] Receiver functions recorded by the 54-station 920 km long Program for Array Seismic Studies of the Continental Lithosphere–Incorporated Research Institutions for Seismology Colorado Plateau/Rio Grande Rift Seismic Transect Experiment (LA RISTRA) line array display a pervasive negative polarity P to S conversion ($P_d s$) arrival preceding the positive polarity 410 km discontinuity arrival. These arrivals are modeled as a low-velocity layer atop the 410 km discontinuity (410-LVL) and are inverted for a velocity profile via a grid search using a five-parameter linear gradient velocity model. Model parameter likelihood and correlations are assessed via calculation of one- and two-dimensional marginal posterior probability distributions. The maximum likelihood model parameter values found are top velocity gradient thickness of 0.0 km with a 4.6% (−0.22 km/s) shear velocity reduction, a 19.8 km constant velocity layer, and bottom gradient thickness of 25.0 km with a 3.5% (+0.17 km/s) shear velocity increase. The estimated mean thickness of the 410-LVL is 32.3 km. The top gradient of the 410-LVL is sharp within vertical resolution limits of P to S conversion (<10 km), and the diffuse 410 km velocity gradient is consistent with hydration of the olivine-wadsleyite phase transformation. The 410-LVL is interpreted as a melt layer created by the Transition Zone Water Filter model. Two secondary observations are found: (1) the 410-LVL is absent from the SE end of the array and (2) an intermittent negative polarity $P_{525}s$ arrival is observed. We speculate that upper mantle shear velocity anomalies above the 410 km discontinuity may manifest Rayleigh-Taylor instabilities nucleated from the 410-LVL melt layer that are being shed upward on time scales of tens of millions of years.

Components: 9241 words, 15 figures, 2 tables.

Keywords: 410 km discontinuity; mantle transition zone; receiver functions.

Index Terms: 8124 Tectonophysics: Earth's interior: composition and state (1212); 1038 Geochemistry: Mantle processes (3621).

Received 9 September 2009; **Revised** 22 December 2009; **Accepted** 24 December 2009; **Published** 12 March 2010.

Jasbinsek, J. J., K. G. Dueker, and S. M. Hansen (2010), Characterizing the 410 km discontinuity low-velocity layer beneath the LA RISTRA array in the North American Southwest, *Geochem. Geophys. Geosyst.*, *11*, Q03008, doi:10.1029/2009GC002836.

1. Introduction

[2] The Transition Zone Water Filter (TZWF) model advocates a new understanding of the genetic significance of the MORB and OIB geochemical signatures found in mantle-derived basaltic composition magmas [*Bercovici and Karato*, 2003]. The model suggests that the upwelling of wet wadsleyite across the 410 km discontinuity may permit a hydrous melt layer to form atop the 410 km discontinuity. The melt layer will sequester incompatible elements resulting in an upwelling residuum with a MORB like composition; thus mitigating the need for a physically distinct upper mantle MORB reservoir. The TZWF requires five necessary and sufficient conditions to operate: (1) wadsleyite has a higher water solubility than olivine, (2) the wadsleyite in the transition zone is >1% hydrated, (3) the mantle flow is upward, (4) the density of the hydrous melt generated is intermediate to the olivine-dominated upper mantle assemblage and the wadsleyite-dominated upper transition zone, and (5) the melt-solid wetting angle is sufficient to create nonzero permeability to permit porous flow within the melt layer [*Bercovici and Karato*, 2003]. Given these conditions, upwelling hydrated transition zone material that crosses the wadsleyite-olivine phase transition at the 410 km discontinuity is predicted to cross the wet solidus and produce a hydrous melt. Additionally, melt layer stability is conditional on water content of the melt; that is, the melt can be positively buoyant with respect to the base of the upper mantle if the melt water content is >7%. Hence buoyant melt-rich diapirs may be shed upward [*Inoue et al.*, 2007; *Sakamaki et al.*, 2006].

[3] A simple global water filter calculation using a background transition zone upwelling rate of ~1 mm/yr predicts a steady state melt layer with a thickness of 2–20 km [*Bercovici and Karato*, 2003]. However, a thicker melt layer could be formed in several ways: (1) increased wadsleyite hydration, (2) increased mantle upflow rates, and (3) the ponding of melt via lateral flow associated with 410 km discontinuity topography [*Karato et al.*, 2006]. A melt layer atop the 410 km discontinuity would be manifest seismically as a low-velocity layer, herein called the "410 low-velocity layer" (410-LVL).

[4] Seismic observations of a 410-LVL beneath North America are found in the Pacific Northwest [*Song et al.*, 2004], northern Mexico [*Gao et al.*, 2006], and the northern Rocky Mountains [*Fee and Dueker*, 2004; *Jasbinsek and Dueker*, 2007]. In addition, magnetotelluric data beneath southern Arizona is modeled as a 5 to 30 km thick high-conductivity layer atop the 410 km discontinuity and interpreted as evidence for a 410-LVL [*Toffelmier and Tyburczy*, 2007]. Globally, a 410-LVL has been observed in eastern China [*Revenaugh and Sipkin*, 1994], Siberia [*Vinnik et al.*, 2003], Arabia [*Vinnik et al.*, 2004], and the SW Pacific [*Thomas and Billen*, 2009]. These previous results find a variable 410-LVL thicknesses of 5–90 km, and a shear velocity reduction of 3–9%. It has been suggested that the 410-LVL may correlate with upwelling plume regions [*Vinnik and Farra*, 2007].

[5] A recent $P_d s$ receiver function study using data recorded at 118 globally distributed stations only infrequently detects evidence of a 410-LVL [*Lawrence and Shearer*, 2006]. Thus, the current set of 410-LVL observations suggests that this layer is intermittent and spatially heterogeneous. In this study, a vertical seismic resolution of 10 km is obtained using 4 s dominant period $P_d s$ arrivals. Stacking waveforms from the relatively high station density Colorado Plateau/Rio Grande Rift Seismic Transect Experiment (LA RISTRA) array data set provides robust error estimates allowing statistical analysis of velocity model fits.

2. Data and Methods

2.1. Array and Earthquake Sources

[6] The Incorporated Research Institutions for Seismology–Program for Array Seismic Studies of the Continental Lithosphere LA RISTRA array was composed of 54 broadband seismic stations deployed at a 17 km spacing to create a 920 km long linear array. The array operated for 18 months across New Mexico, Utah, Arizona and Texas (Figure 1). Teleseismic earthquake locations used in this study provide a good distribution of sources from the NW, SE, and SW back azimuth quadrants (Figure 2). The dense station spacing and excellent distribution of earthquake distances in the NW and SE back azimuth quadrants provide a high fold data set capable of accurately isolating $P_d s$ conversions from velocity discontinuities in the mantle transition zone.

2.2. Source Deconvolution

[7] Receiver function calculation is performed using the Extended-Time MultiTaper method [*Helffrich*, 2006]. This method reduces spectral leakage and finite time series length amplitude bias by using a

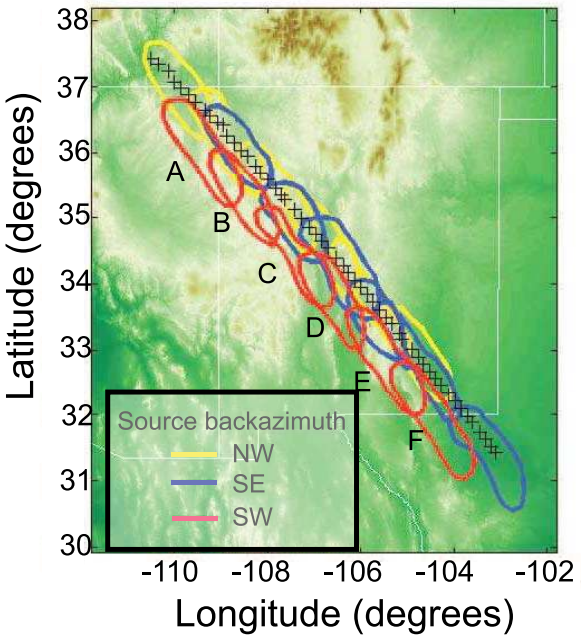

Figure 1. LA RISTRA array stations, ray sampling of 410 km discontinuity, and colored topography. Seismic stations are denoted as black pluses. The $P_{410}s$ piercing points for the back azimuth quadrant bins are outlined in color. The labels A–F correspond to the six quadrant stacks formed in each of the NW, SE, and SW back azimuths.

multitaper spectral estimator and overlapping spectral estimation windows formed from orthogonal Slepian taper functions [*Helffrich*, 2006; *Park*, 1987; *Park and Levin*, 2000]. To stabilize the spectral division in the receiver function calculation the spectrum of preevent noise is used as the spectral water level. After deconvolution, a second-order zero-phase Butterworth band-pass filter with corners at 3 and 30 s is applied to the receiver functions.

2.3. Data and Culling

[8] Teleseismic data recorded by the array are restricted to events at 30°–100° epicentral distance with body wave magnitudes >5.6. Earthquake events are further culled for processing by calculating the amplitude ratio of a short-term (2 s) temporal window (STA) with respect to a long-term (20 s) temporal window (LTA). Events with a STA/LTA ratio >3 are culled to yield 3690 three-component receiver functions.

[9] To investigate back azimuth–dependent P_ds seismic responses, the data are subdivided into the three well-sampled NW, SE, and SW back azimuth quadrants (Figures 1 and 2). Data from each back azimuth quadrant is then divided into six overlapping 185 km wide station bins (quadrant bins) with 50% bin sharing (Figure 1). Data culling within each quadrant bin is performed by correlating all the individual radial receiver functions with the mean radial receiver function in each quadrant bin and rejecting individual receiver functions with a normalized correlation of <0.2. The final data cull is a visual inspection of the receiver functions that removes any harmonic or clearly spurious traces. The final data set consists of 1951 three-component receiver functions. Each quadrant bin contains 59–162 receiver functions and the receiver functions in each bin are linearly stacked to form a total of 18 quadrant bin stacks (Figures 1 and 3). Receiver functions are mapped from time to depth using the western U.S. Tectonic North America shear wave model [*Grand and Helmberger*, 1984]. The V_p/V_s ratio is fixed to the IASP91 velocity model averages of 1.76 in the crust and 1.81 in the mantle.

2.4. Grid Search

[10] To model the interfering and opposite polarity 410 km discontinuity and 410-LVL seismic responses, a simple five-parameter velocity model is used which consists of two linear velocity gradients and a constant velocity layer. The five model parameters are defined as (1) TG, the thickness of the top negative velocity gradient; (2) dV_s-TG, the top negative gradient shear velocity decrement; (3) BG, the thickness of the bottom positive shear velocity gradient; (4) dV_s-BG, the bottom shear

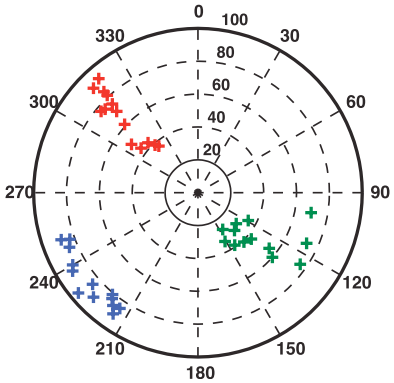

Figure 2. Teleseismic earthquake source distribution. Earthquakes are plotted with respect to back azimuth and great circle distance in degrees. The NW and SE quadrants show an excellent distribution of sources with respect to distance that permits reliable moveout analysis. In the SW quadrant, the event distance range is too limited to warrant a moveout analysis.

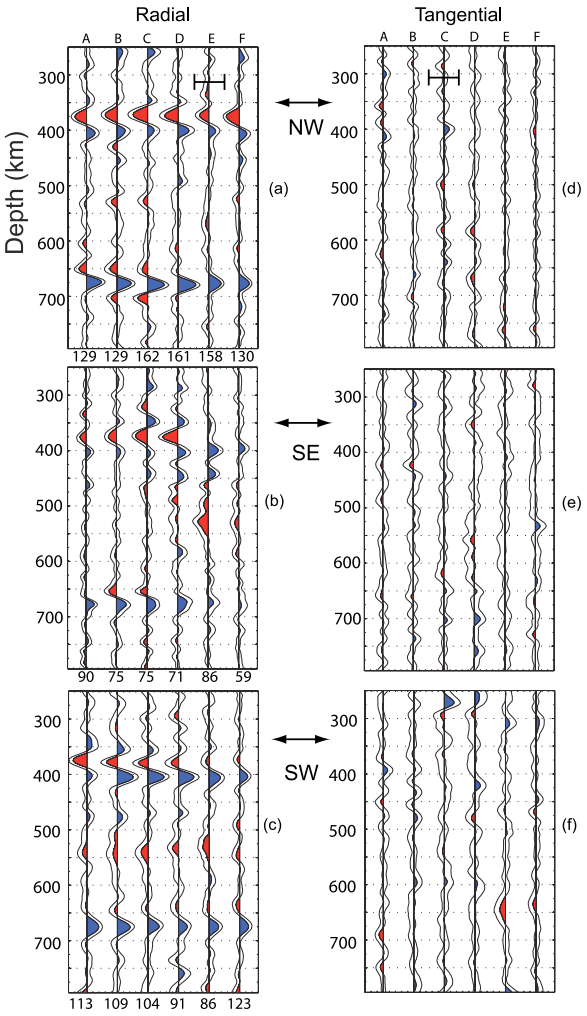

Figure 3. (a–c) Radial and (d–f) tangential receiver functions from NW, SE, and SW back azimuths. Quadrant bins A–F are shown in Figure 1. The number of receiver functions in each bin is indicated at the bottom of each trace. The signal that is greater than one standard deviation is shaded red/blue, and the standard deviation of the signal is indicated as thin black lines. The amplitude scale symbol denotes a 10% variation relative to the vertical P wave amplitude.

velocity gradient increase; and (5) ST, the thickness of a constant velocity layer bounded above and below by the two velocity gradients. The dV_s-BG parameter is defined as the velocity increase in the bottom gradient after recovery of the top gradient velocity decrement (Figure 4a).

[11] To assess the fit of the double-gradient slab model (DGS) with respect to our stacked waveforms, a five dimensional grid search is performed resulting in the calculation of 116,160 synthetic seismograms (Table 1). Synthetic receiver functions are calculated using an isotropic velocity reflectivity code [*Park*, 1996]. Because the tangential receiver functions have low amplitude (<2% relative to vertical P) and no coherence with respect to the radial components, (Figures 3d–3f) this choice of isotropic calculations is reasonable. The mean ray parameter value of the data set is about 0.06 s/km and is used in the synthetic calculations. To account for anelastic effects, the Futterman attenuation operator [*Futterman*, 1962] is applied to the synthetic data. A t^*_{Pds} value of 1.5 s is used assuming a t^*_{P410s} value of 2 s and a t^*_{P410p} value of 0.5 s [*Liu*, 2003]. Application of this attenuation operator results in a small amplitude decrease of the main pulse and a slight broadening of pulse widths.

[12] Since we are interested in modeling waveform shapes and not the absolute timing of the waveforms, the synthetics are cross correlated with the waveform stacks to find the optimal temporal alignment. The lag time of the peak of the cross correlation function is used to shift the observed and synthetic waveforms into relative alignment. Both the L^2 and cross-correlation norms have been used as a misfit function, but these two norms show little difference in the posterior probability density functions. Thus, the L^2 norm is used because it permits Gaussian statistics to be used and posterior probability density functions may be calculated.

2.5. Marginal Posterior Probability Density Function Integration

[13] A Gaussian likelihood function is used to quantify the fit of each model to the data:

$$L(m) = k \exp\left(-\frac{1}{2}(d - g(m))^T C_D^{-1}(d - g(m))\right),$$

where d is the observed receiver function vector, m is the double gradient slab model vector, $g(m)$ is the synthetic receiver function for a given model m, C_D^{-1} is the inverse data covariance matrix [*Sambridge*, 1999], and k is an arbitrary scaling constant, taken to equal 1. The probability of a model m given a data vector d is calculated as $P(m|d) = k\rho(m)L(m|d)$ where k is a second arbitrary scaling factor and $\rho(m)$ is the a priori probability distribution of the model parameters. In this study all models are considered equally likely a priori, i.e., $\rho(m) = 1$; hence, the probability and likelihood functions are simply rescaled versions of each other and the probability function $P(m)$ is replaced by the likelihood function $L(m)$.

[14] To visualize the five-dimensional error volume defined by $L(m)$, the 1- and 2-D marginal proba-

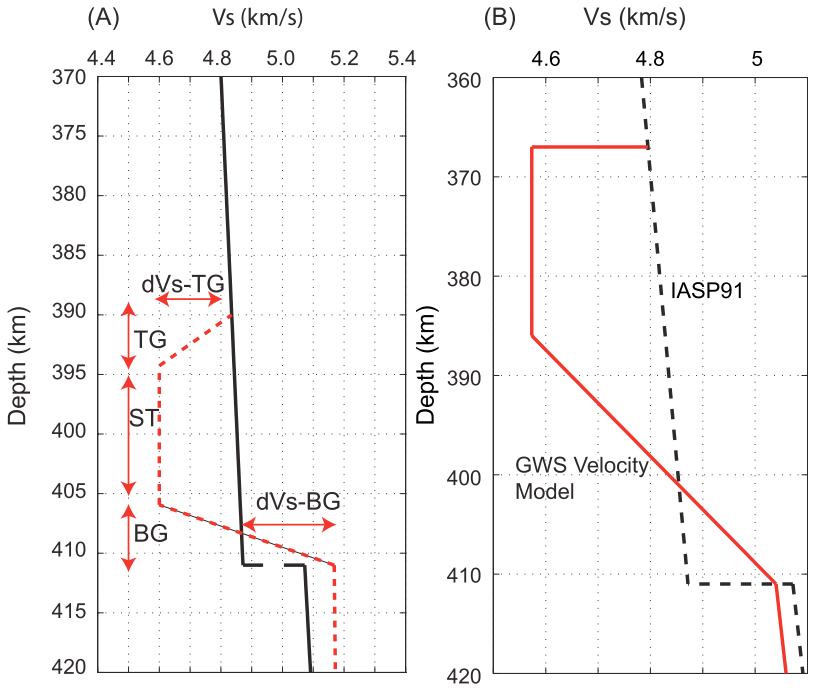

Figure 4. Double gradient slab (DGS) model parameterization. (a) The solid black line is the IASPI91 shear velocity model, and the dashed red lines indicate a trial DGS velocity model. The five model parameters are as follows: TG, top gradient thickness (km); ST, constant velocity slab thickness (km); BG, bottom gradient thickness (km); dVs-TG, shear wave velocity decrease for the top gradient (km/s); and dVs-BG, shear wave velocity increase in the bottom gradient (km/s). The value of dVs-BG is the velocity increase after the top gradient velocity decrement is recovered. (b) IASPI shear velocity model and maximum likelihood DGS velocity model for the Global Waveform Stack (GWS) (Figure 6). The velocity model is characterized by a sharp top velocity gradient and diffuse bottom velocity gradient.

bility distributions are computed for each model parameter and pairs of model parameters (Figure 5). The 1-D marginal probability distribution function for the *i*th model parameter is defined as

$$M_1(m_i) = \int \cdots \int P(m) \prod_{\substack{k=1 \\ k \neq i}}^{n} dm_k,$$

where n is the number of DGS model parameters (five). The 2-D marginal probability distributions between the *i*th and *j*th model parameter are similarly defined as

$$M_2(m_i, m_j) = \int \cdots \int P(m) \prod_{\substack{k=1 \\ k \neq i,j}}^{n} dm_k.$$

[15] The 1-D marginal probability distributions indicate how well a model parameter is resolved: a compact unimodal distribution indicates a well-resolved model parameter. The 2-D marginal probability distributions display the correlation between pairs of model parameters. To test our calculation of the marginal probability distributions, synthetic data with an additive normally distributed noise with a standard error equal to that measured in the culled data set are created. Our calculation of posterior marginal probability density functions recovers near-exact parameter values of the synthetic velocity model when applied to this synthetic data.

3. Results

[16] To characterize the trade-off between spatial bin size and observed back azimuth–dependent

Table 1. Parameter Value Ranges for the Double-Gradient Slab Model

Parameter	Minimum	Increment	Maximum
TG (km)	0	5	45
BG (km)	0	5	35
ST (km)	0	5	55
dV_s-TG (km/s)	−0.80	0.08	0
dV_s-BG (km/s)	0	0.17	1.7

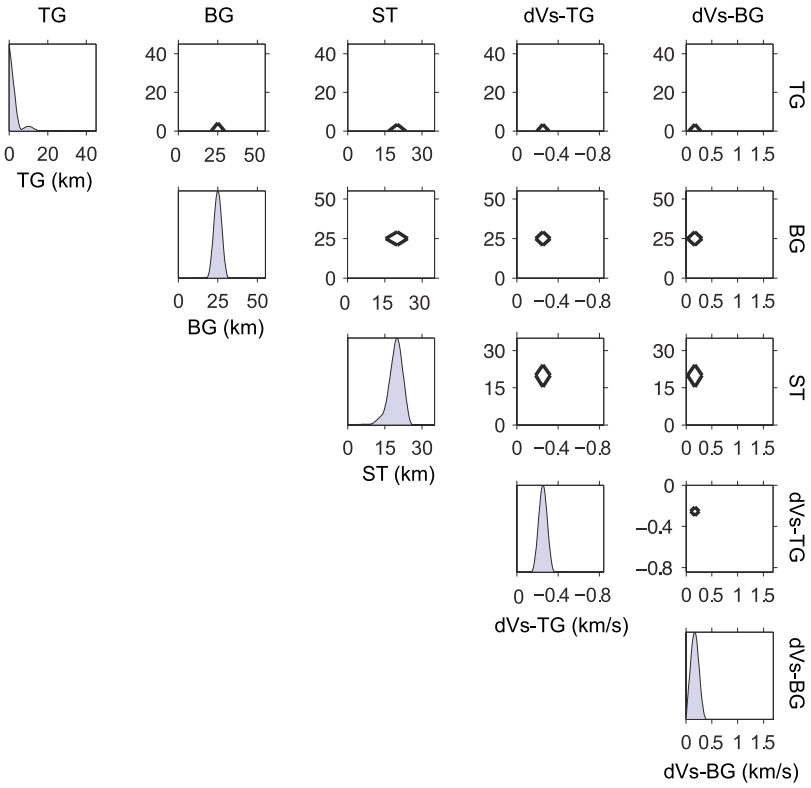

Figure 5. Global waveform stack 1- and 2-D marginal probability distributions for the five double gradient slab model parameters. The model parameters are denoted as follows: TG, top gradient; BG, bottom gradient; ST, slab thickness; dVs-TG, top shear velocity step; dVs-BG, bottom shear velocity step. The 1-D distributions are shown along the diagonal of the upper half "matrix," and the 2-D distributions are the "off-diagonal matrix" elements. The 1-D distributions are unimodal and compact, indicating well-resolved model parameters. The 2-D distributions are contoured at the 99% probability level and show that the model parameters are uncorrelated.

P_ds responses, three different spatial scale stacks are presented: the stack of all 1951 receiver functions termed the global waveform stack, the stacks of the receiver functions by back azimuth quadrant bin termed quadrant stacks, and a common conversion point (CCP) image [*Dueker and Sheehan*, 1997] that uses 80 km wide bins. Each of the three analyses shows the presence of a negative polarity P_ds arrival interfering with the P_{410}s arrival.

3.1. Global Waveform Stack

[17] The global waveform stack of all 1951 radial receiver functions shows a clear negative polarity P_ds arrival (410-LVL arrival) preceding and interfering with the positive polarity P_{410}s arrival (Figure 6a). The 1-D marginal probability distributions for the DGS model are highly peaked (Figure 5), demonstrating that the DGS model (Figure 4) is an adequate velocity model parameterization. The DGS maximum likelihood parameter values are: a top gradient thickness of 0 km; a top gradient shear velocity decrement of 0.22 km/s; a bottom gradient thickness of 25 km; a bottom gradient shear velocity increase of 0.17 km/s; and a constant velocity layer thickness of 19.8 km (Figure 4b). The 2-D marginal posteriori probability distributions show tightly peaked functions indicative of little trade-off between the five model parameters (Figure 5). Thus, the DGS model parameterization provides a very good fit to the mean stacked waveform (Figure 6b) with a reduced chi square value of 1.3. The thickness of the 410-LVL is estimated as the constant velocity layer thickness plus half the sum of the top and bottom gradient thicknesses: i.e., 32.3 km (Figure 4b). With respect to the IASPI91 velocity model, the top gradient shear velocity decrement is 4.6% (−0.22 km/s) and the bottom shear velocity increment is 3.5% (0.17 km/s).

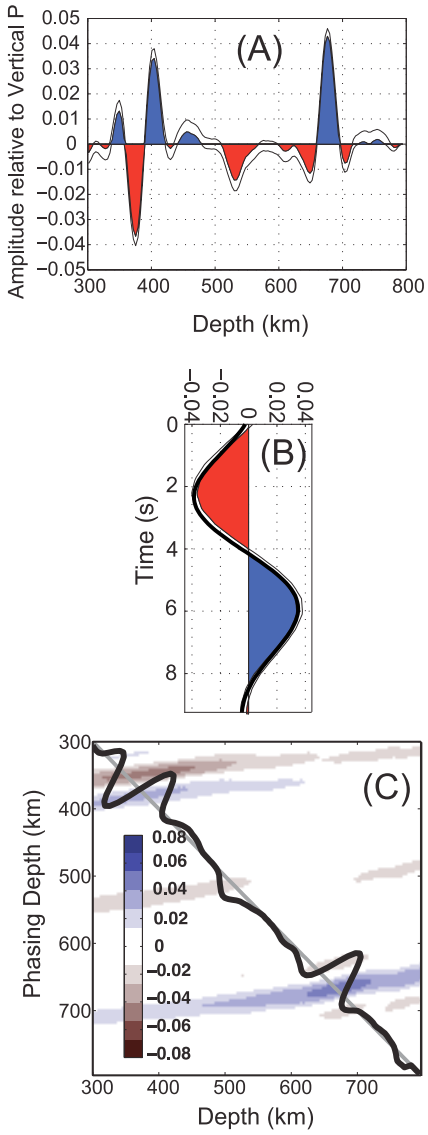

Figure 6. Global waveform stack analysis. (a) Global waveform stack (shaded red/blue) and standard deviation error lines. (b) Windowed global waveform stack 410 and 410-LVL and model fit. The maximum likelihood model values (i.e., the peaks of the marginal probability distributions in Figure 5) are used to calculate the synthetic seismogram denoted as the thickened black line. The reduced chi-square value of the synthetic model is 1.3. (c) Moveout/phasing characteristics of the 410-LVL, 410, and 660 km discontinuity. The unity slope gray line shows the line of predicted P_ds moveout at which the amplitude of P to S conversions should be maximal. The results demonstrate that the 410-LVL, 410, and 660 km discontinuities display the correct P_ds moveout.

3.2. Quadrant Stacks

[18] In each back azimuth quadrant bin, the receiver function data are linearly stacked to form quadrant stacks labeled as A–F (Figures 1 and 3). Inspection of the radial component quadrant stacks shows that the 410 and 660 km discontinuity arrivals are accurately isolated (Figure 3). The waveform of the 660 km discontinuity arrival is coherent across the quadrant bins and the peak amplitude of the arrival is consistent with the predicted IASP91 $P_{660}s$ arrival amplitude of 3% relative to vertical P. The 410 km discontinuity arrival amplitude and pulse width is more variable and are discussed below. In addition, the SE quadrant stacks for bins C–E (Figure 3b) show a set of positive arrivals at 440 km that are underlain by an irregular set of small negative polarity arrivals. However, these secondary arrivals are not observed in the NW and SW back azimuth quadrants (Figures 3a and 3c).

[19] The tangential component quadrant stacks contain low amplitudes of <2% with respect to the direct P wave, consistent with the absence of significant anisotropic velocity contrasts or dipping layers (Figures 3d–3f). Where tangential energy is observed, no coherence is observed with respect to the radial component quadrant stacks. This observation suggests that the effects of velocity anisotropy and dipping layers may be ignored in our analysis.

[20] Above the 410 km discontinuity arrival, negative polarity $P_{375}s$ (410-LVL) arrivals are observed on 14 out of the 18 radial receiver function quadrant stacks. Generally, the 410-LVL arrivals have equal or greater amplitude with respect to the 410 km discontinuity arrival. The most notable spatial variation of the 410-LVL arrival is its disappearance at the SE end of the array beneath SW Texas and SE New Mexico (Figures 3b, 3c, 7, and 8).

[21] From the quadrant stacks, the measured depth range of the 410 km discontinuity is 389–406 km (17 km variation) with a mean of 403 km and the depth range of the 660 km discontinuity is 673–679 km (6 km variation) with a mean of 676 km (Table 2). The errors associated with these depth estimates are assessed via bootstrapping [*Efron and Tibshirani*, 1994]. This error analysis finds the standard deviation of the discontinuity depths is generally <3 km. However, this error analysis only quantifies the error in isolating the peak arrival time of the discontinuity arrivals. The uncertainty in the absolute discontinuity depths are contingent upon the accuracy of the assumed P and S wave velocity model used to migrate the receiver function from time to depth. Using reasonable variations in our P and S wave velocity model [*Bedle*

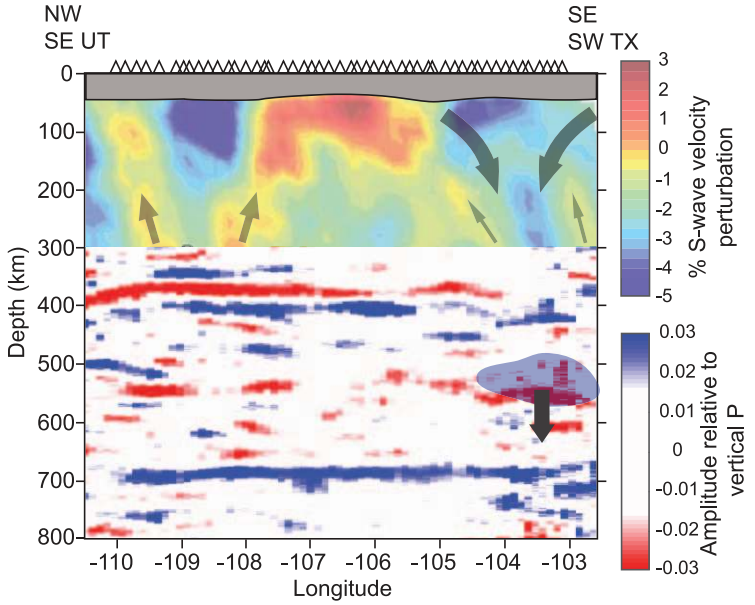

Figure 7. P_ds common conversion point image and a shear wave tomogram produced from the LA RISTRA array [*Sine et al.*, 2008]. Crustal depth is indicated by the grey shaded region [*Wilson and Aster*, 2005]. The down arrows indicate regions of potential downwelling due to lithospheric edge delamination [*Song and Helmberger*, 2007], and the up arrows indicate regions of potential upwelling associated with low velocity mantle anomalies. Multiple arrivals beneath the 660 km discontinuity at the SE edge of the image are not interpreted due to the reduced sampling at the edge of the image.

and van der Lee, 2009; *Burdick et al.*, 2008, 2009; *Sine et al.*, 2008] the absolute discontinuity depths are estimated to be accurate to within ±5 km. Thus the 410 and 660 km discontinuities are 15 and 16 km shallower and deeper, respectively, than averages (418 km and 660 km) beneath the North American southwest [*Flanagan and Shearer*, 1998b].

[22] Because the magnitude of velocity anomalies in the transition zone are generally much smaller with respect to the upper 200 km, the mean 271 km transition zone thickness beneath the array is considered a robust estimate. This estimate is 11.5% thicker than the global average of 243 km [*Gu and Dziewonski*, 2002], suggesting a cold and/or hydrated transition zone [*Bolfan-Casanova et al.*, 2006; *Courtier and Revenaugh*, 2006; *Frost and Dolejs*, 2007; *Hirschmann et al.*, 2005; *Litasov et al.*, 2006; *Wood*, 1995].

[23] To quantify variations in velocity characteristics of the 410-LVL within the array, the NW quadrant stacks are modeled with the double-gradient slab model (Figure 4 and Table 1). The NW quadrant stacks are used because they contain the most receiver functions per bin (mean of 145) and the simplest 410-LVL waveforms (Figure 3a). An overlay of the maximum likelihood double-gradient slab model synthetic waveforms generally fit within one standard deviation of the stacked waveforms with reduced chi-square values of 0.5–8.2 (Figure 9). The double gradient slab 1-D marginal probability functions for the NW quadrant stack bins (Figure 10) show that the velocity steps for the top and bottom velocity gradients are very consistent (−0.37 km/s and 0 km/s, respectively). For the top velocity gradient thickness, four of the six 1-D marginal probability distributions have a peak probability density at 0 km thickness; whereas for the bottom gradient thickness, the six marginal probability distributions are centered near 22 km. The constant velocity slab (ST) marginal probability distributions are the most variable, indicating lateral variations in the thickness of the 410-LVL.

[24] The SW quadrant stack bins E and F (Figure 3c) lack a 410-LVL arrival and hence provide a simpler seismic response with which to constrain the 410 km discontinuity velocity step. Modeling of the waveforms from these two bins finds a bottom gradient thickness of 16.7 and 30.0 km and a shear velocity increment of 0.51 and 0.49 km/s, respectively (Figure 11). As expected due to the lack of a

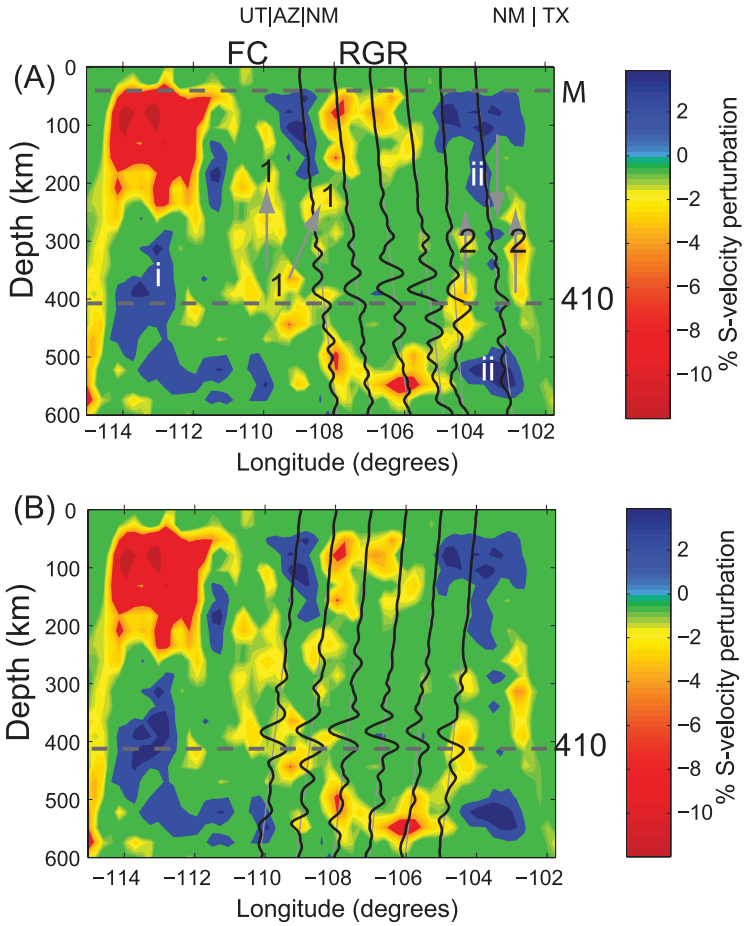

Figure 8. Overlay of quadrant stack traces and S wave tomogram of *Sine et al.* [2008]. (a) NW quadrant stack overlay (see also Figure 3a). (b) SE quadrant stack overlay (see also Figure 3b). The scale bar displays the tomographic S wave velocity perturbations. Receiver functions (black lines) are oriented such that positive polarity is to the right. The quadrant stack waveforms are traced to depth from the middle of each bin at the surface (Figure 1) using an average ray parameter of 0.06 s/km. Quadrant stack waveform amplitudes are muted above 200 km depth. Labels denote the following: M, Moho; 410, 410 km discontinuity; RGR, Rio Grande Rift; FC, Four Corners region. Labels 1 and 2 indicate regions of low S velocity above the 410 km depth, and grey arrows indicate potential flow direction. Label i is interpreted in previous studies as a Farallon slab fragment, and label ii is a possible delaminated volume of lithosphere.

410-LVL arrival, the double-gradient slab modeling recovers a model with no velocity decrement at the top. Yet, the estimated 410 km discontinuity shear velocity increase is twice the IASP91 predicted value of 0.23 km/s. These large amplitude $P_{410}s$ arrivals are likely focused arrivals from local 410 km discontinuity topography and thickness variations and/or near surface amplification effects [*van der Lee et al.*, 1994].

3.3. Common Conversion Point Image

[25] A common conversion point (CCP) image of the 1951 receiver functions images the 410 and 660 and 410-LVL discontinuities (Figure 7). In addition, an intermittent negative polarity arrival is found at 520–560 km depth. The 660 km discontinuity arrival is coherently imaged with mean amplitude of 3% with respect to the P component amplitude beneath the stations where data fold is good. The 660 km discontinuity image finds no evidence of significant topography. The most notable change in the 410 km discontinuity signal is found beneath SE New Mexico and SW Texas; here, the CCP image finds that the 410-LVL arrival is absent. This spatial variation in the 410-LVL arrival is also observed in the SE and SW quadrant stacks (Figures 3b and 3c).

Table 2. Depths and Errors for the 410 and 660 Discontinuities

Quadrant Stack	d410 (km)	d410, σ (km)	d660 (km)	d660, σ (km)
NW_A	405.0	3.0	673.8	1.7
NW_B	401.6	2.9	676.5	1.9
NW_C	401.1	4.1	679.0	1.5
NW_D	400.4	2.6	679.3	1.2
NW_E	401.3	2.9	676.8	2.2
NW_F	406.3	2.5	676.7	2.6
SE_A	403.0	3.9	677.9	2.1
SE_B	404.0	6.3	678.5	2.9
SE_C	405.0	5.1	677.8	4.6
SE_D	403.3	3.5	675.5	5.9
SE_E	405.9	3.1	674.5	2.5
SE_F	397.0	4.5	676.0	9.6
SW_A	402.5	4.1	675.5	2.8
SW_B	404.6	2.0	675.6	2.0
SW_C	404.2	1.5	674.1	3.3
SW_D	404.5	1.6	675.2	4.1
SW_E	406.0	3.0	674.7	2.7
SW_F	403.4	2.6	674.1	3.2
Mean	403.3	3.3	676.2	3.2

[26] Noteworthy is that a previous study of the LA RISTRA 410 and 660 km discontinuities only found weakly intermittent 410-LVL arrivals [*Wilson et al.*, 2005b; *Wilson and Aster*, 2005] with much less lateral coherence than the images presented herein. This difference in the lateral coherence of the 410-LVL arrival is attributed to different culling of the data and the larger bin sizes used in our receiver function quadrant stacks.

3.4. Negative Polarity $P_{525}s$ Arrivals

[27] Our global waveform stack finds a 2% negative polarity amplitude arrival at about 525 km depth. This arrival is prominent in the SW quadrant stacks and intermittently in the NW and SE quadrant stacks at 520–550 km depth (Figure 3). In addition, the CCP image intermittently images this arrival in the 530–550 km range (Figure 7). Due to the lower signal-to-noise ratio of this arrival, the moveout characteristics are not as well resolved as the 410-LVL, $P_{410}s$ and $P_{660}s$ arrivals (Figures 6c and A1). The proximity of the observed 525 km arrival to the nominal depth of the wadsleyite-ringwoodite phase transformation (520 km discontinuity) is discussed below.

4. Discussion

[28] Several seismic velocity effects could explain the origin of the 410-LVL. First, velocity anisotropy due to lattice preferred orientation just above the 410 km discontinuity could produce low velocities for selected wave directions. However, the tangential receiver function stacks have small amplitudes and no spatial coherency consistent with velocity anisotropy (Figure 3). Therefore, velocity anisotropy is rejected as a cause of the 410-LVL. Second, a subsolidus chemical anomaly with respect to an assumed pyrolitic mantle, such as accumulated oceanic crust separated from its underlying mantle lithosphere [*Lee and Chen*, 2007] could create a low-velocity anomaly. Yet, tomographic images of the upper mantle and transition zone in the study area do not support the presence of oceanic crust atop the transition zone [*Bedle and van der Lee*, 2009; *Burdick et al.*, 2008, 2009; *Sine et al.*, 2008]. Therefore, the 410-LVL is interpreted as a hydrous melt layer created by the Transition Zone Water Filter [*Bercovici and Karato*, 2003].

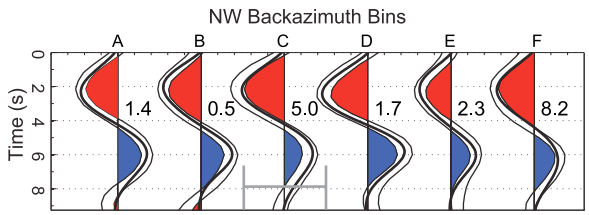

Figure 9. Overlay of maximum likelihood double gradient slab model synthetic and observed waveforms for the NW event back azimuth quadrant. Numbers adjacent to each trace are the reduced chi-square values for model fit to data. The gray scale bar represents 10% amplitude variation relative to vertical P. The maximum likelihood model fits the peaks and troughs of the observed data within the one-sigma error bars.

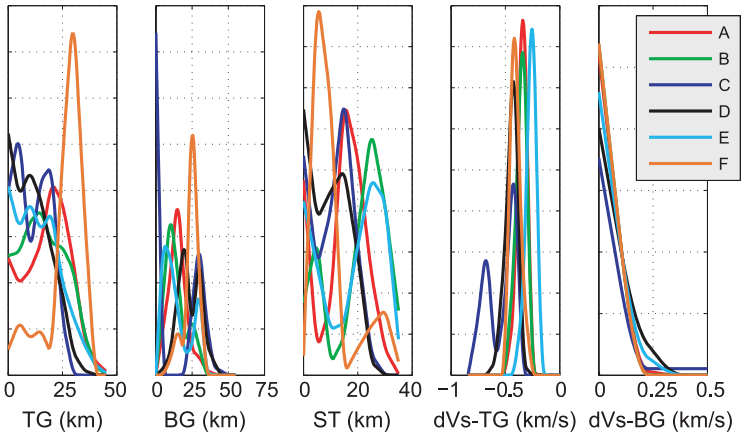

Figure 10. Overlay of the NW quadrant stack A–F binned waveform 1-D marginal probability distributions for the double gradient slab model (Figure 4a). The model parameters are denoted as follows: TG, top gradient; BG, bottom gradient; ST, slab thickness; dVs-TG, top shear velocity step; dVs-BG, bottom shear velocity step. The colored lines (A–F) correspond to the stacking bins (A–F) shown in Figure 1. The peaks of the 1-D marginal probability distribution functions define the maximum likelihood parameter values for the double gradient slab velocity models.

4.1. Transition Zone Thickness

[29] The olivine-wadsleyite transformation (410 km velocity discontinuity) is predicted to occur at lower pressure and over a broader pressure interval under hydrous conditions [*Frost and Dolejs*, 2007; *Hirschmann et al.*, 2005, 2006; *Litasov et al.*, 2006; *Smyth and Frost*, 2002; *Wood*, 1995]. Although results vary based on experimental method, starting material composition and water content, the results of *Litasov et al.* [2006] are an illustrative example: in hydrous pyrolite containing ~3 wt % H_2O the olivine-wadsleyite transformation is estimated to occur at 0.5 GPa (15 km) lower pressure, with a significant broadening of the transformation pressure interval to 1.2 GPa (36 km). This is broadly consistent with our finding of 16 and 30 km wide olivine-wadsleyite transition thicknesses in quadrant stacks SW-E and SW-F, respectively (Figures 3 and 11), and 410 km discontinuity depths decreased by 12 and 14.6 km from the 418 km average in the North American southwest [*Flanagan and Shearer*, 1998a]. Conversely, the 660 km discontinuity is predicted to occur at higher pressure in a hydrous versus anhydrous environment [*Bolfan-Casanova et al.*, 2003, 2006]. One study estimates the 660 km discontinuity onset pressure is increased by 0.6–1 GPa (18–30 km) in hydrous pyrolite [*Litasov et al.*, 2006], consistent with our mean observed 660 km discontinuity depth of 676.2 km (Table 2). Thus, the larger than average transition zone thickness found here may be explained by perturbations of both nominal 410 and 660 km discontinuity depths via a hydrated upper and lower mantle transition zone. A possible mechanism for transporting water into the transition zone is via subducting slabs. Dense hydrous magnesium silicates found in subducting slabs transform into superhydrous phase B and phase D at transition zone pressures [*Irifune et al.*, 1998; *Kohlstedt et al.*, 1996; *Shieh et al.*, 1998];

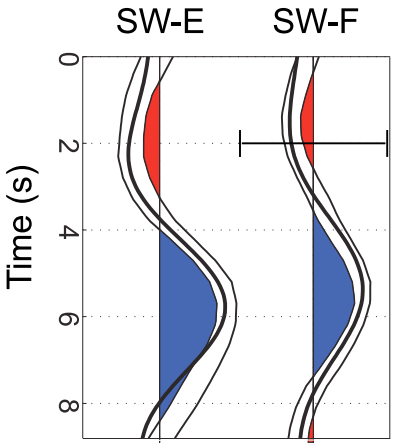

Figure 11. Maximum likelihood models for SW-E and SW-F quadrant bin stacks that do not have a significant 410-LVL arrival. The black scale bar represents 10% amplitude relative to vertical P. For the SW-E and SW-F bins, bottom velocity gradient thicknesses of 16.7 km and 30.0 km and shear velocity increases of 0.51 km/s and 0.49 km/s, respectively, are found by the double gradient slab model fitting.

thus, these phases may provide the necessary transport mechanism.

[30] Temperature perturbations also modulate the onset pressure of the 410 and 660 km discontinuities [*Bolfan-Casanova et al.*, 2006; *Frost and Dolejs*, 2007; *Hirschmann*, 2006; *Hirschmann et al.*, 2005; *Katsura et al.*, 2004], with colder temperatures decreasing/increasing the pressures at which the 410/660 km discontinuities occur. Applying a Clapeyron slope of 3 MPa/K for the 410 km discontinuity, the maximum temperature decrease required to explain the up to 14.6 km shallower than normal 410 km discontinuity depths in the SW-E and SW-F quadrant stacks is 163°C. Similarly, a temperature decrease of 600–1200°C is required to explain the mean 660 km discontinuity with a Clapeyron slope of −1 to −0.5 MPa/K. Tomographic images of the mantle beneath North America are consistent with the presence of slab fragments in the transition zone [*Bedle and van der Lee*, 2009; *Burdick et al.*, 2008; *Roth et al.*, 2008; *Sine et al.*, 2008], which could explain lower than normal mantle transition zone temperatures. However, detailed temperature perturbations in the transition zone beneath the linear 2-D LA RISTRA array are not resolvable.

4.2. Negative Polarity $P_{525}s$ Arrivals

[31] Negative polarity $P_{525}s$ arrivals (Figures 3, 6a, and 7) cannot be explained by any known solid state phase transformations in the transition zone. In particular, the 520 km discontinuity, which is generally associated with the wadsleyite-ringwoodite phase transformation, is a positive velocity step with respect to increasing depth [*Helffrich and Wood*, 2001] thus creating a positive polarity P-S conversion. The dominant mantle transition zone minerals, wadsleyite and ringwoodite, have higher water solubility than the dominant upper (olivine) and lower (perovskite + ferropericlase) mantle minerals [*Bolfan-Casanova et al.*, 2002, 2003; *Hirschmann et al.*, 2005; *Murakami et al.*, 2002]. These solubility contrasts may cause the mantle transition zone to act as a mantle water reservoir [*Karato et al.*, 2006].

[32] Similar to the olivine-wadsleyite phase transition at the 410 km discontinuity and the ringwoodite-perovskite phase transition at the 660 km discontinuity, the wadsleyite-ringwoodite phase transition demarks a change in water solubility [*Bolfan-Casanova et al.*, 2006]. However, the direction of the decrease in water solubility across the 520 km phase transition is potentially opposite with respect to the 410 km phase transition: water solubility may be locally greater in the shallower wadsleyite region (up to 3.2 wt% H_2O) than in the deeper ringwoodite region (up to 2.7 wt%) [*Bolfan-Casanova et al.*, 2006; *Inoue et al.*, 1998; *Kohlstedt et al.*, 1996; *Ohtani et al.*, 2000]. Thus, a downward flux of sufficiently hydrated wadsleyite across the 520 km phase transition would require repartitioning of the water [*Karato et al.*, 2006]. The exsolved water may sufficiently lower the solidus of ringwoodite to produce either hydrous melt or free water vapor [*Karato et al.*, 2006]. If true, then a negative polarity P_ds arrival could be produced.

[33] An important difference between the 410 km discontinuity water filter and a potential 520 km discontinuity water filter is that no density contrast exists for the melt to gravitationally perch upon. Thus, assuming the melt produced is positively buoyant, it would percolate upward. Given the uncertainties in the potential for hydrous melting across the wadsleyite-ringwoodite phase boundary and melt density about the 520 km discontinuity, this interpretation is speculative. We note also that negative polarity P_ds arrivals have been observed at 570–600 km depths in the transition zone beneath southern Africa [*Shen and Blum*, 2003]. These arrivals were modeled as a 2.2% shear velocity reduction and interpreted as evidence for accumulated oceanic crust above the 660 km discontinuity.

4.3. Buoyant Upwelling From the 410 Low-Velocity Layer

[34] A dynamical question with respect to the hydrous melt layer atop the 410 km discontinuity is its gravitational stability [*Leahy and Bercovici*, 2007]. To first order the gravitational stability of a 410 melt layer depends on the melt layer thickness and the hydrous melt density contrast with respect to the upper mantle [*Leahy and Bercovici*, 2007; *Youngs and Bercovici*, 2009]. The hydrous melt density and viscosity are strong functions of water content. Experimental results find that in a pyrolitic assemblage melt production at 1400°C with 6.7 wt% water forms a gravitationally stable hydrous melt perched atop the 410 km discontinuity density gradient [*Matsukage et al.*, 2005; *Sakamaki et al.*, 2006]. However, a gravitationally unstable layer is produced at temperatures of 1400°C and water content of 10 wt% in the melt. Thus, the development of a Rayleigh-Taylor instability from a sufficiently thick and water-rich 410 melt layer is plausible [*Inoue et al.*, 2007].

[35] The temporal evolution of a Rayleigh-Taylor instability from the 410-LVL would depend on the volume of positively buoyant melt layer that is available to feed the instability. Gravitational segregation of the hydrous melt layer would segregate the most water rich, hence buoyant, melt to the top of the melt layer. If sufficient volume is available, an upwelling plume-like diapir may be expected as buoyant melt forces the growing instability [*Youngs and Bercovici*, 2009]. Eventually, a growing instability may locally exhaust available buoyant melt volume leading to a detachment of the diapir from the 410-LVL.

[36] Assuming the top 20 km of the 32.3 km thick 410-LVL found by our analysis is gravitationally unstable, the dominant wavelength of the R–T instability is predicted to be ~50 km [*Turcotte and Schubert*, 2002; *Youngs and Bercovici*, 2009]. A 50 km diameter spherical diapir volume would require advection of a 20 km thick layer over a 3250 km^2 area (57 km wide square). Assuming a 10% melt solid density contrast and a 10^{20}Pa s mantle viscosity, a Stokes Flow estimate [*Turcotte and Schubert*, 2002] of melt volume transit time to the base of the lithosphere is on the order of 10 million years.

[37] A S wave tomogram constructed from the LA RISTRA array data [*Sine et al.*, 2008] (Figures 7 and 8) defines many low-velocity anomalies in the upper mantle and transition zone. The first set of velocity anomalies is centered at −109° longitude and originates near the 410 km discontinuity (labeled 1 in Figure 8a). These velocity anomalies reside near the Four-Corners and Jemez caldera just west of the Rio Grande Rift. The second set of velocity anomalies above 410 km depth reside at −104° longitude (labeled 2 in Figure 8a) [*Sine et al.*, 2008]. The maximum shear velocity decrease in region 1 is ~3%, corresponding to a 1.4% melt porosity using standard upper mantle melt velocity scaling relations [*Kreutzmann et al.*, 2004]. Using the same scaling relations, the 4.6% shear velocity reduction at the 410-LVL corresponds to 2.1% melt porosity. Therefore, a rising diapir from the 410-LVL could possess sufficient melt porosity to account for the observed shear velocity reductions. We speculate that these low-velocity anomalies in the upper mantle may be ascending diapirs shed from the 410-LVL melt layer.

[38] Finally, it is remarkable that the 410-LVL is absent from beneath SW Texas and SE New Mexico (Figures 3, 7, and 8). Assuming that the fast material in the transition zone is delaminated lithosphere [*Song and Helmberger*, 2007], then the 410 melt layer, assuming it had been previously developed, has either (1) advected downward beneath the sinking lithospheric volume or (2) flowed laterally due to the pressure associated with the sinking lithospheric volume as it transited the 410 km discontinuity.

[39] Buoyantly ascending hydrous melt diapirs ("water pipes") may be an explanation for the low-velocity anomalies above 410 km discontinuity beneath the Rio Grande Rift and the Four-Corners area (Figure 8) [*Wilson et al.*, 2005a]. The impact of buoyant hydrous melt diapirs on 10 million year time ascent scales beneath the Rio Grande Rift could provide potential gravitational energy to promote extension of the lithosphere [*Jones et al.*, 1996; *Wilson et al.*, 2005a]. Further high-resolution seismic imaging of the upper mantle beneath this region may allow this "water pipe" hypothesis to be tested.

5. Conclusions

[40] This study has constrained the thickness and velocity characteristics of a low-velocity layer atop the 410 km discontinuity (410-LVL) beneath the southern Rocky Mountains with a dense array data set. The 410-LVL is found to be 32.3 km thick with a sharp top velocity gradient with a mean 4.6% shear velocity reduction. These results are interpreted as a manifestation of the Transition Zone Water Filter model that has created a layer of hydrous melt atop the 410 km discontinuity. The receiver function data also isolates a negative polarity P_ds conversion at 525 km. We speculate this results from a hydrous melting process similar to the TZWF model. Comparison of the 410-LVL results with S wave tomography from the LA RISTRA Array [*Sine et al.*, 2008] suggests the 410-LVL may be shedding buoyant hydrous melt diapirs that ascend upward to impact the base of the lithosphere.

Appendix A

A1. Moveout and Resampling Analysis

[41] The P_{410}s, P_{660}s and $P_{410\text{-}LVL}$s arrivals from the NW and SE back azimuth quadrants all display the correct moveout for P_ds arrivals (Figure A1).

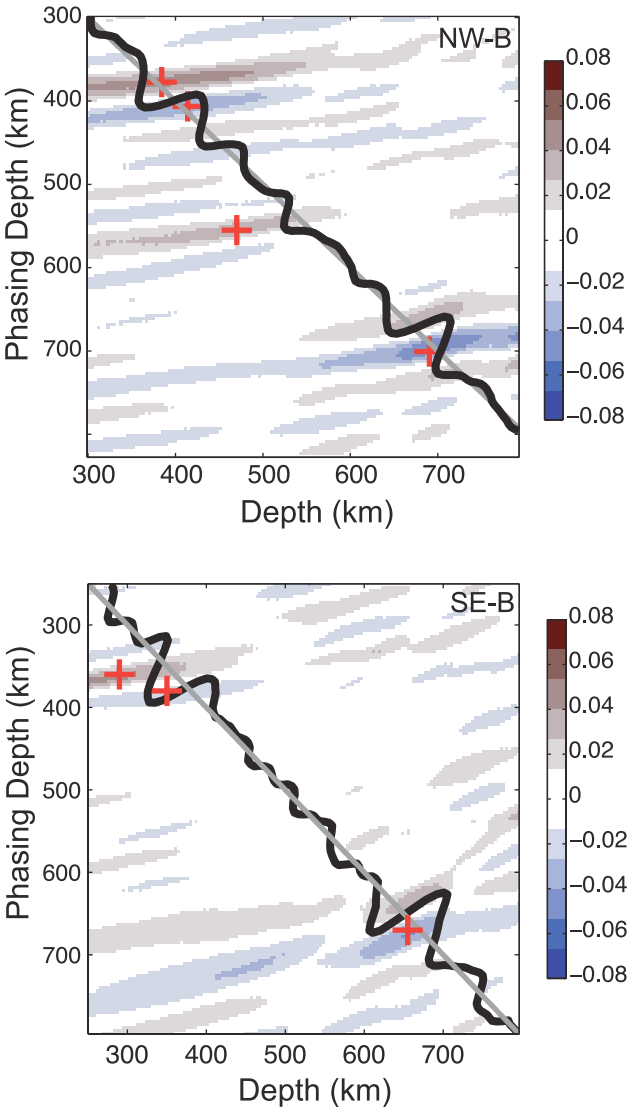

Figure A1. P_ds moveout/phasing analysis for quadrant stack bins NW-B and SE-B. Each radial receiver function is mapped from time to depth with the 1-D velocity model described in the Data and Culling section. The unity slope gray lines show where the phasing depth equals the mapped depth, and the amplitude of P to S conversions should be maximal. The solid black lines are the P_ds moveout corrected traces (same as Figure 3). The red pluses correspond to the maximal phasing amplitude. The results demonstrate that the 410-LVL, 410, and 660 km discontinuity arrivals display the correct P_ds moveout for these two selected bins.

Sources from the SW back azimuth are not well distributed with respect to distance (Figure 2), and thus this quadrant does not permit moveout analysis. To test the robustness of our quadrant stacks, the data is divided into two random and disjoint halves (Figure A2) and then restacked. This data division analysis shows that a random half of the total data set is sufficient to constrain the waveshape of the P_ds arrivals. The plots for other data bins (not shown) are similar.

A2. Source Deconvolution and Filtering Effects

[42] To account for the filtering effects associated with the deconvolution and the postdeconvolution

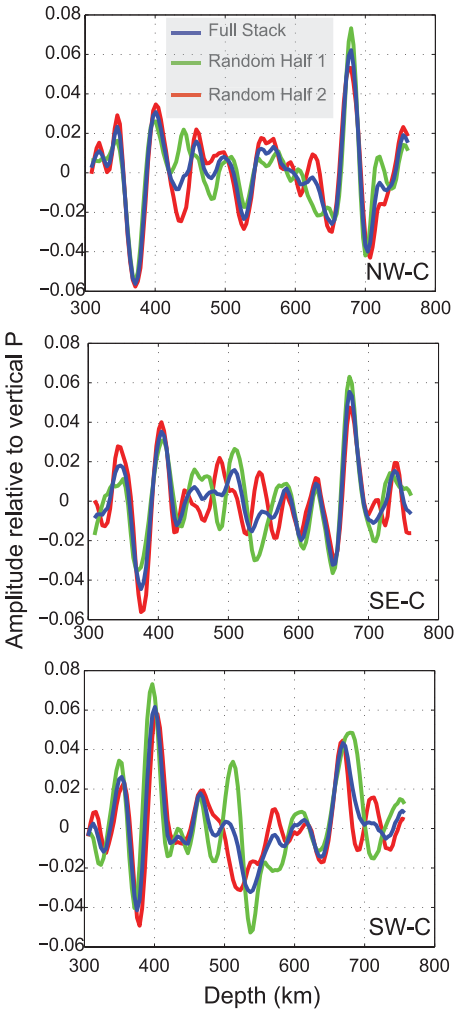

Figure A2. Random-half receiver function quadrant stacks for bins NW-C, SE-C, and SW-C. The blue trace is the mean receiver function stack, and the two disjoint random data halves are plotted as red and green lines. These representative examples demonstrate that the 410-LVL, 410, and 660 km discontinuity signals are robustly isolated by disjoint halves of the data set.

filter, the mean estimated impulse response is calculated by stacking all deconvolved and filtered vertical component receiver functions (Figure A3). The first side lobes are 20% of the main peak amplitude. This mean impulse response is convolved with our synthetic seismograms to facilitate direct comparison with the observed data.

A3. Marginal Posterior Probability Density Function Integration

[43] To test whether the observed receiver function data are normally distributed, normal cumulative probability plots are calculated for the peak times of the 410 km discontinuity and 410-LVL arrivals (Figure A4). These plots show that within nearly two standard deviations of the mean (10% and 90% probability on the ordinate) the data are normally distributed. In contrast, beyond 10% and 90% normal probability, the data contains "fat" probability tails with respect to a theoretical Gaussian tail. These fat tails will thus make our standard deviation estimates greater than that predicted by a true normal distribution. With this caveat noted, we conclude that our data are sufficiently normally distributed to warrant the use of the L^2 norm to quantify misfit.

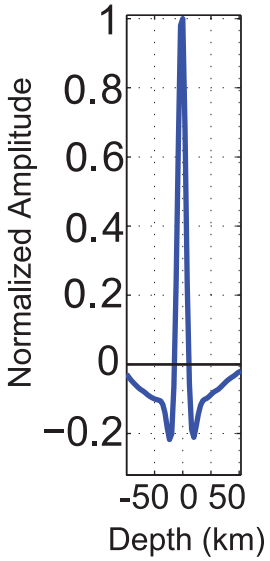

Figure A3. Mean stacked waveform of the vertical receiver functions. This wavelet is convolved with the synthetic seismograms to account for the filtering and deconvolution effects in the processed data.

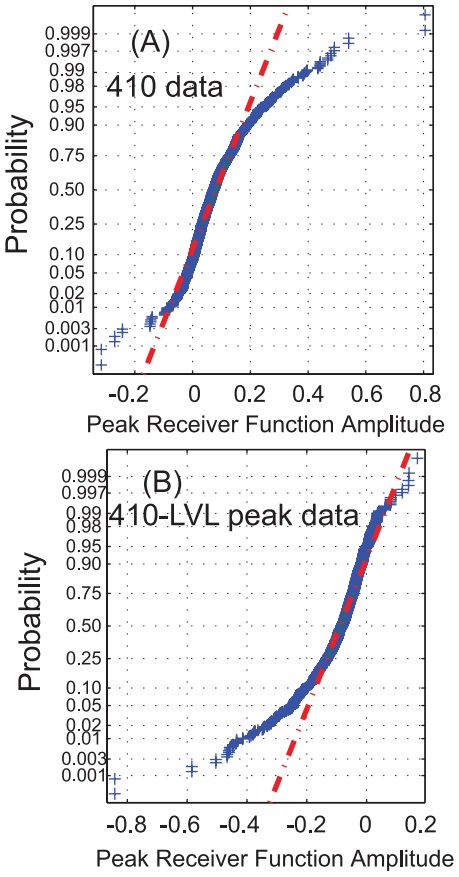

Figure A4. Data normality test. A Gaussian probability distribution was fit to data samples at the peaks of the discontinuity arrivals. (a) The 410 km discontinuity. (b) The 410-LVL. If the data were normally distributed, the data would plot along the red dashed line. The slope of the red line is proportional to the standard deviation of the data, and the data value at which the line crosses 0.5 probability is the Gaussian mean of the data. The data follow a normal distribution between approximately 10%–90% probability, after which the distribution has fat tails with respect to a Gaussian distribution.

Acknowledgments

[44] The authors would like to acknowledge two anonymous reviewers for thoughtful reviews and constructive comments, which improved the manuscript. We also acknowledge the facilities of the IRIS Data Management System, and specifically the IRIS Data Management Center, for access to the waveform and metadata required in this study.

References

Bedle, H., and S. van der Lee (2009), *S* velocity variations beneath North America, *J. Geophys. Res.*, *114*, B07308, doi:10.1029/2008JB005949.

Bercovici, D., and S. Karato (2003), Whole-mantle convection and the transition-zone water filter, *Nature*, *425*, 39–44, doi:10.1038/nature01918.

Bolfan-Casanova, N., S. J. Mackwell, H. Keppler, C. A. McCammon, and D. C. Rubie (2002), Pressure dependence of H solubility in magnesiowüstite up to 25 GPa: Implications for the storage of water in the Earth's lower mantle, *Geophys. Res. Lett.*, *29*(10), 1449, doi:10.1029/2001GL014457.

Bolfan-Casanova, N., H. Keppler, and D. C. Rubie (2003), Water partitioning at 660 km depth and evidence for very low water solubility in magnesium silicate perovskite, *Geophys. Res. Lett.*, *30*(17), 1905, doi:10.1029/2003GL017182.

Bolfan-Casanova, N., C. A. McCammon, and S. J. Mackwell (2006), Water in transition zone and lower mantle minerals, in *Earth's Deep Water Cycle*, *Geophys. Monogr. Ser.*, vol. 168, edited by S. D. Jacobsen and S. van der Lee, pp. 57–68, AGU, Washington, D. C.

Burdick, S., C. Li, V. Martynov, T. Cox, J. Eakins, T. Mulder, L. Astiz, F. L. Vernon, G. L. Pavlis, and R. D. van der Hilst (2008), Upper mantle heterogeneity beneath North America from travel time tomography with global and USArray transportable array data, *Seismol. Res. Lett.*, *79*(3), 384–392, doi:10.1785/gssrl.79.3.384.

Burdick, S., R. D. van der Hilst, F. L. Vernon, V. Martynov, T. Cox, J. Eakins, T. Mulder, L. Astiz, and G. L. Pavlis (2009), Model update December 2008: Upper mantle heterogeneity beneath North America from P wave travel time tomography with global and USArray transportable array data, *Seismol. Res. Lett.*, *80*(4), doi:10.1785/gssrl.80.4.638.

Courtier, A. M., and J. Revenaugh (2006), A water-rich transition zone beneath the eastern United States and Gulf of Mexico from multiple ScS reverberations, in *Earth's Deep Water Cycle*, *Geophys. Monogr. Ser.*, vol. 168, edited by S. D. Jacobsen and S. van der Lee, pp. 181–193, AGU, Washington, D. C.

Dueker, K. G., and A. F. Sheehan (1997), Mantle discontinuity structure from midpoint stacks of converted P and S waves across the Yellowstone hotspot track, *J. Geophys. Res.*, *102*(B4), 8313–8327, doi:10.1029/96JB03857.

Efron, B., and R. J. Tibshirani (1994), *An Introduction to the Bootstrap*, Chapman and Hall, New York.

Fee, D., and K. Dueker (2004), Mantle transition zone topography and structure beneath the Yellowstone hotspot, *Geophys. Res. Lett.*, *31*, L18603, doi:10.1029/2004GL020636.

Flanagan, M. P., and P. M. Shearer (1998a), Topography on the 410-km seismic velocity discontinuity near subduction zones from stacking sS, sP, and pP precursors, *J. Geophys. Res.*, *103*(B9), 21,165–21,182.

Flanagan, M. P., and P. M. Shearer (1998b), Global mapping of topography on transition zone velocity discontinuities by stacking SS precursors, *J. Geophys. Res.*, *103*(B3), 2673–2692, doi:10.1029/97JB03212.

Frost, D. J., and D. Dolejs (2007), Experimental determination of the effect of H_2O on the 410-km seismic discontinuity, *Earth Planet. Sci. Lett.*, *256*(1–2), 182–195, doi:10.1016/j.epsl.2007.01.023.

Futterman, W. I. (1962), Dispersive body waves, *J. Geophys. Res.*, *73*, 3917–3935.

Gao, W., E. Matzel, and S. P. Grand (2006), Upper mantle seismic structure beneath eastern Mexico determined from P and S waveform inversion and its implications, *J. Geophys. Res.*, *111*, B08307, doi:10.1029/2006JB004304.

Grand, S. P., and D. V. Helmberger (1984), Upper mantle shear structure of North America, *Geophys. J. R. Astron. Soc.*, *76*, 399–438.

Gu, Y. J., and A. M. Dziewonski (2002), Global variability of transition zone thickness, *J. Geophys. Res.*, *107*(B7), 2135, doi:10.1029/2001JB000489.

Helffrich, G. (2006), Extended-time multitaper frequency domain cross-correlation receiver-function estimation, *Bull. Seismol. Soc. Am.*, *96*(1), 344–347, doi:10.1785/0120050098.

Helffrich, G. R., and B. J. Wood (2001), The Earth's mantle, *Nature*, *412*(6846), 501–507, doi:10.1038/35087500.

Hirschmann, M. M. (2006), Water, melting, and the deep Earth H_2O cycle, *Annu. Rev. Earth Planet. Sci.*, *34*, 629–653, doi:10.1146/annurev.earth.34.031405.125211.

Hirschmann, M. M., C. Aubaud, and A. C. Withers (2005), Storage capacity of H_2O in nominally anhydrous minerals in the upper mantle, *Earth Planet. Sci. Lett.*, *236*(1–2), 167–181, doi:10.1016/j.epsl.2005.04.022.

Hirschmann, M. M., A. C. Withers, and C. Aubaud (2006), Petrologic structure of a hydrous 410 km discontinuity, in *Earth's Deep Water Cycle*, *Geophys. Monogr. Ser.*, vol. 168, edited by S. D. Jacobsen and S. van der Lee, pp. 277–287, AGU, Washington, D. C.

Inoue, T., J. B. Parise, D. J. Weidner, and P. A. Northrup (1998), Elastic properties of hydrous ringwoodite (gamma phase) in Mg_2SiO_4, *Earth Planet. Sci. Lett.*, *160*(1–2), 107–113, doi:10.1016/S0012-821X(98)00077-6.

Inoue, T., K. Kojima, and T. Irifune (2007), Water content of magma generated just above the 410-km discontinuity, *Eos Trans. AGU*, *88*(52), Fall Meet. Suppl., Abstract V24A-06.

Irifune, T., et al. (1998), The postspinel phase boundary in Mg_2SiO_4 determined by in situ X-ray diffraction, *Science*, *279*(5357), 1698–1700, doi:10.1126/science.279.5357.1698.

Jasbinsek, J., and K. G. Dueker (2007), Ubiquitous low-velocity layer atop the 410-km discontinuity in the northern Rocky Mountains, *Geochem. Geophys. Geosyst.*, *8*, Q10004, doi:10.1029/2007GC001661.

Jones, C. H., J. R. Unruh, and L. J. Sonder (1996), The role of gravitational potential energy in active deformation in the southwestern United States, *Nature*, *381*(6577), 37–41, doi:10.1038/381037a0.

Karato, S., D. Bercovici, G. Leahy, G. Richard, and Z. Jing (2006), The transition-zone water filter model for global material circulation: Where do we stand?, in *Earth's Deep Water Cycle*, *Geophys. Monogr. Ser.*, vol. 168, edited by S. D. Jacobsen and S. van der Lee, pp. 289–313, AGU, Washington, D. C.

Katsura, T., et al. (2004), Olivine-wadsleyite transition in the system $(Mg, Fe)_2SiO_4$, *J. Geophys. Res.*, *109*, B02209, doi:10.1029/2003JB002438.

Kohlstedt, D. L., H. Keppler, and D. C. Rubie (1996), Solubility of water in the ALPHA, BETA and GAMMA phases of $(Mg, Fe)_2SiO_4$, *Contrib. Mineral. Petrol.*, *123*, 345–357, doi:10.1007/s004100050161.

Kreutzmann, A., G. Marquart, I. T. Bjarnason, H. Schmeling, A. Junge, and T. Ruedas (2004), Temperature and melting of a ridge-centred plume with application to Iceland. Part II: Predictions for electromagnetic and seismic observables, *Geophys. J. Int.*, *159*(3), 1097–1111, doi:10.1111/j.1365-246X.2004.02397.x.

Lawrence, J. F., and P. M. Shearer (2006), A global study of transition zone thickness using receiver functions, *J. Geophys. Res.*, *111*, B06307, doi:10.1029/2005JB003973.

Leahy, G. M., and D. Bercovici (2007), On the dynamics of a hydrous melt layer above the transition zone, *J. Geophys. Res.*, *112*, B07401, doi:10.1029/2006JB004631.

Lee, C.-T. A., and W.-P. Chen (2007), Possible density segregation of subducted oceanic lithosphere along a weak serpen-

tinite layer and implications for compositional stratification of the Earth's mantle, *Earth Planet. Sci. Lett.*, *255*(3–4), 357–366, doi:10.1016/j.epsl.2006.12.022.

Litasov, K. D., E. Ohtani, and A. Sano (2006), Influence of water on major phase transitions in the Earth's mantle, *Earth's Deep Water Cycle*, *Geophys. Monogr. Ser.*, vol. 168, edited by S. D. Jacobsen and S. van der Lee, pp. 95–111, AGU, Washington, D. C.

Liu, K. H. (2003), Effects of inelasticity on the apparent depth and detectibility of seismic discontinuities in the mantle, *Geophys. Res. Lett.*, *30*(9), 1455, doi:10.1029/2002GL015264.

Matsukage, K. N., Z. Jing, and S. Karato (2005), Density of hydrous silicate melt at the conditions of the Earth's deep upper mantle, *Nature*, *438*, 488–491, doi:10.1038/nature04241.

Murakami, M., K. Hirose, H. Yurimoto, S. Nakashima, and N. Takafuji (2002), Water in Earth's lower mantle, *Science*, *295*, 1885–1887, doi:10.1126/science.1065998.

Ohtani, E., H. Mizobata, and H. Yurimoto (2000), Stability of dense hydrous magnesium silicate phases in the systems Mg_2SiO_4–H_2O and $MgSiO_3$–H_2O at pressures up to 27 GPa, *Phys. Chem. Miner.*, *27*, 533–544, doi:10.1007/s002690000097.

Park, J. (1987), Multitaper spectral analysis of high-frequency seismograms, *J. Geophys. Res.*, *92*(B12), 12,675–12,684, doi:10.1029/JB092iB12p12675.

Park, J. (1996), Surface waves in layered anisotropic structures, *Geophys. J. Int.*, *126*, 173–184, doi:10.1111/j.1365-246X.1996.tb05276.x.

Park, J., and V. Levin (2000), Receiver functions from multitaper spectral correlation estimates, *Bull. Seismol. Soc. Am.*, *90*(6), 1507–1520, doi:10.1785/0119990122.

Revenaugh, J., and S. A. Sipkin (1994), Seismic evidence for silicate melt atop the 410-km mantle discontinuity, *Nature*, *369*(6480), 474–476, doi:10.1038/369474a0.

Roth, J. B., M. J. Fouch, D. E. James, and R. W. Carlson (2008), Three-dimensional seismic velocity structure of the northwestern United States, *Geophys. Res. Lett.*, *35*, L15304, doi:10.1029/2008GL034669.

Sakamaki, T., A. Suzuki, and E. Ohtani (2006), Stability of hydrous melt at the base of the Earth's upper mantle, *Nature*, *439*(7073), 192–194, doi:10.1038/nature04352.

Sambridge, M. (1999), Geophysical inversion with a Neighbourhood Algorithm—II, *Geophys. J. Int.*, *138*, 727–746, doi:10.1046/j.1365-246x.1999.00900.x.

Shen, Y., and J. Blum (2003), Seismic evidence for accumulated oceanic crust above the 660-km discontinuity beneath southern Africa, *Geophys. Res. Lett.*, *30*(18), 1925, doi:10.1029/2003GL017991.

Shieh, S. R., H. Mao, R. J. Hemley, and L. C. Ming (1998), Decomposition of phase D in the lower mantle and the fate of dense hydrous silicates in subducting slabs, *Earth Planet. Sci. Lett.*, *159*, 13–23, doi:10.1016/S0012-821X(98)00062-4.

Sine, C. R., D. Wilson, W. Gao, S. P. Grand, R. Aster, J. Ni, and W. S. Baldridge (2008), Mantle structure beneath the western edge of the Colorado Plateau, *Geophys. Res. Lett.*, *35*, L10303, doi:10.1029/2008GL033391.

Smyth, J. R., and D. J. Frost (2002), The effect of water on the 410-km discontinuity: An experimental study, *Geophys. Res. Lett.*, *29*(10), 1485, doi:10.1029/2001GL014418.

Song, T. A., and D. V. Helmberger (2007), P and S waveform modeling of continental sub-lithospheric detachment at the eastern edge of the Rio Grande Rift, *J. Geophys. Res.*, *112*, B07319, doi:10.1029/2007JB004942.

Song, T. A., D. V. Helmberger, and S. P. Grand (2004), Low velocity zone atop the 410 seismic discontinuity in the northwestern United States, *Nature*, *427*, 530–533, doi:10.1038/nature02231.

Thomas, C., and M. I. Billen (2009), Mantle transition zone structure along a profile in the SW Pacific: Thermal and compositional variations, *Geophys. J. Int.*, *176*, 113–125, doi:10.1111/j.1365-246X.2008.03934.x.

Toffelmier, D. A., and J. A. Tyburczy (2007), Electromagnetic detection of a 410-km-deep melt layer in the southwestern United States, *Nature*, *447*(7147), 991–994, doi:10.1038/nature05922.

Turcotte, D. L., and G. Schubert (2002), *Geodynamics*, 2nd ed., Cambridge Univ. Press, Cambridge, U. K.

van der Lee, S., H. Paulssen, and G. Nolet (1994), Variability of P660s phases as a consequence of topography of the 660 km discontinuity, *Phys. Earth Planet. Inter.*, *86*(1–3), 147–164, doi:10.1016/0031-9201(94)05066-X.

Vinnik, L., and V. Farra (2007), Low S velocity atop the 410-km discontinuity and mantle plumes, *Earth Planet. Sci. Lett.*, *262*(3–4), 398–412, doi:10.1016/j.epsl.2007.07.051.

Vinnik, L., M. R. Kumar, R. Kind, and V. Farra (2003), Superdeep low-velocity layer beneath the Arabian plate, *Geophys. Res. Lett.*, *30*(7), 1415, doi:10.1029/2002GL016590.

Vinnik, L. P., V. Farra, and R. Kind (2004), Deep structure of the Afro-Arabian hotspot by S receiver functions, *Geophys. Res. Lett.*, *31*, L11608, doi:10.1029/2004GL019574.

Wilson, D., and R. Aster (2005), Seismic imaging of the crust and upper mantle using regularized joint receiver functions, frequency–wave number filtering, and multimode Kirchhoff migration, *J. Geophys. Res.*, *110*, B05305, doi:10.1029/2004JB003430.

Wilson, D., S. Grand, W. Gao, W. S. Baldridge, S. Semken, P. Patel, R. Aster, M. West, and J. Ili (2005a), Lithospheric structure of the Rio Grande rift, *Nature*, *433*(7028), 851–855, doi:10.1038/nature03297.

Wilson, D., M. West, W. Gao, W. S. Baldridge, S. Semken, R. Aster, J. Ni, and S. Grand (2005b), Imaging the seismic structure of the crust and upper mantle beneath the Great Plains, Rio Grande Rift, and Colorado Plateau using receiver functions, *J. Geophys. Res.*, *110*, B05306, doi:10.1029/2004JB003492.

Wood, B. J. (1995), The effect of H_2O on the 410-kilometer seismic discontinuity, *Science*, *268*, 74–76, doi:10.1126/science.268.5207.74.

Youngs, B. A. R., and D. Bercovici (2009), Stability of a compressible hydrous melt layer above the transition zone, *Earth Planet. Sci. Lett.*, *278*, 78–86, doi:10.1016/j.epsl.2008.11.024.